US Army Corps of Engineers®
Engineer Research and
Development Center

CuO Enhances the Photocatalytic Activity of Fe₂O₃ through Synergistic Reactive Oxygen Species Interactions

Emily Asenath-Smith, Emma K. Ambrogi, Eftihia Barnes, and Jonathon A. Brame

September 2021

Engineer Research and
Development Center

CuO Enhances the Photocatalytic Activity of Fe₂O₃ through Synergistic Reactive Oxygen Species Interactions

Emily Asenath-Smith and Emma K. Ambrogi

Cold Regions Research and Engineering Laboratory
U.S. Army Engineer Research and Development Center
72 Lyme Road
Hanover, NH 03755

Efithia Barnes

Geotechnical and Structures Laboratory
U.S. Army Engineer Research and Development Center
3909 Halls Ferry Road
Vicksburg, MS 39180

Jonathan Brame

Environmental Laboratory
U.S. Army Engineer Research and Development Center
3909 Halls Ferry Road
Vicksburg, MS 39180

Final report

Preface

CuO enhances the photocatalytic activity of Fe2O3 through synergistic reactive oxygen species interactions

GRAPHICAL ABSTRACT

ABSTRACT

Iron oxide (α-Fe$_2$O$_3$, hematite) colloids were synthesized under hydrothermal conditions and investigated as catalysts for the photodegradation of an organic dye under broad-spectrum illumination. To enhance photocatalytic performance, Fe$_2$O$_3$ was combined with other transition-metal oxide (TMO) colloids (e.g., CuO and ZnO), which are sensitive to different regions of the solar spectrum (far visible and ultraviolet, respectively), using a ternary blending approach for compositional mixtures. For a variety of ZnO/Fe$_2$O$_3$/CuO mole ratios, the pseudo-first-order rate constant for methyl orange degradation was at least double the sum of the individual Fe$_2$O$_3$ and CuO rate constants, indicating there is an underlying synergy governing the photocatalysis reaction with these combinations of TMOs. A full compositional study was carried out to map the interactions between the three TMOs. Additional experiments probed the identity and role of reactive oxygen species and elucidated the mechanism by which CuO enhanced Fe$_2$O$_3$ photodegradation while ZnO did not. The increased photocatalytic performance of Fe$_2$O$_3$ in the presence of CuO was associated with hydroxyl radical ROS, consistent with heterogeneous photo-Fenton mechanisms, which are not accessible by ZnO. These results imply that low-cost photocatalytic materials can be engineered for high performance under solar illumination by selective pairing of TMOs with compatible ROS.

1. Introduction

The presence of molecular contaminants, such as pharmaceuticals, pesticides, and personal care products, in water supplies is a growing challenge [1,2]. These contaminants tend to persist through conventional wastewater treatment processes, thus meriting their identification as *recalcitrant* contaminants [3,4]. Even in trace amounts, these contaminants can have negative effects on the environment (e.g., aquatic life) [5,6] and on public health [7]. Photodegradation with semiconducting transition-metal oxides (TMOs) presents an appealing method to remediate these contaminants [8–10], but only niche applications of such photocatalytic technologies have been realized [11–13].

Semiconductor photocatalysis proceeds by a cascade of chemical reactions. After absorption of a photon, a valence-band electron is excited to the conduction band generating an electron-hole pair [16,17]. This pair can migrate to the material surface, where it reacts with surrounding water and dissolved oxygen to form reactive oxygen species (ROS). It is these ROS that participate in the redox reactions that lead to the degradation of contaminants. The dominant type of ROS is determined by the photocatalyst bandgap energy and position in relation to the redox energies of oxygen species [18]. For example, photoreactions that are catalyzed by titanium dioxide (TiO_2) under ultraviolet (UV) illumination involve formation of superoxide ($O_2^{\bullet-}$) and hydroxyl radical ($HO^{\bullet}$) ROS, while photoreactions with doped TiO_2 under visible irradiation can form different ROS, including singlet oxygen ($^1O_2$) [19,20].

Largely, the limitations on TMO photocatalysts stem from low photoconversion efficiencies due to poor (visible) light absorption and/or high recombination rates of the photogenerated charge carriers (electrons/holes), which inhibit their participation in surface chemical reactions [14,15]. In a semiconductor, formation of photogenerated charge carriers requires that the energy of incident absorbed photons must at least match the bandgap of the semiconductor [16]. Thus, when a single semiconductor is illuminated with a broad-spectrum light, which includes significant spectral components below the semiconductor's bandgap energy, a large amount of the incident radiation is not utilized.

One approach to increase photoconversion efficiencies is to widen the material's absorption towards the visible region, where greater (solar) spectral irradiance exists [11]. Methods to accomplish this include doping [21–23], dye sensitization [24], formation of heterojunctions with smaller band gap semiconductors [25–28], or use of noble metals [29–34]. In particular, core-shell structures with Au or Ag paired with a TMO have shown enhanced photocatalytic activity as the plasmon resonance of the metal injects electrons to the conduction band of the oxide, enhancing ROS generation pathways [29,35,36]. These advanced materials show enticing structures and properties; however, most require complicated synthesis procedures, which are difficult to commercialize.

Since the earliest work of Kay, Cesar, and Gratzel [37], hematite (iron (III) oxide, α-Fe_2O_3) has shown great potential in solar-activated catalytic processes [38,39], with performance enhancements achieved through hierarchical structuring [40–44], doping [45], and engineered nanostructures [38,39,46]. Seeking a simple route to enhance the photocatalytic activity of Fe_2O_3 under solar illumination, we paired Fe_2O_3 colloids with other TMOs that are sensitive to longer and shorter wavelengths of the solar spectrum. In particular, we investigated organic dye photodegradation by Zn, Fe, and Cu TMO colloidal mixtures, hypothesizing that any observed rate enhancements would be correlated to increased light harvesting afforded by the presence of TMOs absorbing in different regions of the solar spectrum.

Herein we report on the enhanced photocatalytic performance of colloidal Fe_2O_3 achieved by pairing it with other TMOs —UV active zinc oxide (ZnO) [47,48] and near-infrared active copper oxide (CuO) [49,50]. We used nontoxic earth-abundant TMOs, synthesized under mild hydrothermal conditions [51–54], and employed methyl orange (MO) as a model contaminant probe molecule. When pairing Fe_2O_3 with CuO, the MO degradation rate constant more than doubled when compared to that achieved with only Fe_2O_3. We identified a mechanism consistent with compatible pairing of like ROS and heterogeneous photo-Fenton chemistries.

2. Material and methods

2.1. Materials

All reagents were used as received without further purification: zinc nitrate hexahydrate (purum p.a., cyrstallized, ≥99.0 %; Sigma Aldrich); hexamethylenetetramine (ACS Reagent, ≥99.0 %; Sigma Aldrich); iron (III) chloride hexahydrate (puriss. p.a., Reagent Ph. Eur., ≥99 %; Sigma Aldrich); sodium phosphate monobasic dihydrate (purum p.a., crystallized, ≥99.0 %; Sigma Aldrich); copper(II) nitrate trihydrate (purum p.a., 98 %–103 %; Sigma Aldrich); sodium hydroxide (Certified ACS Reagent; Fisher Scientific); hydrogen peroxide (H_2O_2, 30 %; Fisher Scientific); methyl orange (Reagent Ph. Eur.; Sigma Aldrich); titanium dioxide (TiO_2, P25, Sigma Aldrich). All solutions were made using 12 MΩ MilliQ water.

2.2. ZnO synthesis

Particles of ZnO were synthesized hydrothermally in aqueous solution according to procedures described in the literature [55]. In a typical synthesis, 95 mL of 0.016 M zinc nitrate hexahydrate was stirred and heated to 100 °C. Hexamethylenetetramine (HMTA; 0.210 g, 0.00150 mol) was dissolved in 5 mL of water and added to the reaction mixture. The reaction mixture was heated while stirring for 90 min. and was then cooled and filtered to collect the precipitated ZnO particles, which were washed with water (2x) and ethanol (1x) and then dried under vacuum.

2.3. Fe₂O₃ synthesis

Spindle-type Fe_2O_3 particles were prepared as described by Frandsen et al. [56]. Iron (III) chloride hexahydrate (1.08 g, 0.020 mol) was dissolved in a solution of monosodium phosphate (200 mL, 0.09 mM). The solution was placed in a sealed glass media vessel and aged at 100 °C for 2 weeks. Following aging, the solution was cooled, and the precipitated Fe_2O_3 colloids were collected via vacuum filtration, washed with water and ethanol, and then dried under vacuum.

2.4. CuO synthesis

Particles of CuO were synthesized hydrothermally in aqueous solution using procedures previously reported in literature [57,58]. In a typical synthesis, 50 mL of 0.1 M copper nitrate trihydrate were combined with 50 mL 0.1 M HMTA and stirred while heating to 100 °C. Once heated, 8 mL 1 M NaOH were added to the reaction mixture. The reaction mixture was heated for an additional 90 min. After cooling, the precipitated CuO particles were collected via vacuum filtration, rinsed with water (2x) and ethanol (1x), and dried under vacuum.

2.5. Illumination system

A broad-spectrum illumination system based on two tungsten halogen lamps (ASI Illuminator, 50 W each) was used to supply light to the photocatalytic experiments. The illuminators were placed on tripods and pointed at a stir plate on which a glass jacketed beaker was placed (Fig. S1). The lamps were positioned 35 cm above the stir plate and 30 cm apart from each other. Lamps were angled such that beams were directed at the center of the stir plate and were allowed to warm up for at least 5 min. before each reaction. The incident spectral

irradiance (Fig. S2) was measured with a calibrated spectroradiometer (Model HR-1024i, range 340–2500 nm, Spectra Vista Corp., USA) and a calibrated diffuse reflectance target (Spectralon, Labsphere, USA) [59].

2.6. Photocatalytic reactions

In a typical photocatalytic reaction, 30 mg of the photocatalyst was added to an aqueous solution of MO (40 mL, 25 mM) in a glass jacketed beaker, which was maintained at 20 °C. A quartz disk was placed on top of the beaker. The mixture of photocatalyst and contaminant was stirred in the dark (protected from any light exposure) for 30 min to allow for adsorption-desorption equilibrium between the MO and the photocatalyst particles, after which time a 1.5 mL aliquot was withdrawn (t = 0 min point). Then 100 μL of H_2O_2 was immediately added, and the beaker was illuminated. Aliquots (1.5 mL) were taken every 15 min for 1 h (4 aliquots) for analysis by UV–vis spectroscopy (UV–vis). Aliquots were filtered through 0.20 μm filters (Millex PTFE) to remove the photocatalyst and then placed in a quartz cuvette (for UV–vis analysis) [60].

2.7. Materials characterization instrumentation

The TMO photocatalyst samples were dispersed in ethanol and drop-cast onto silicon wafers for imaging in a scanning electron microscope (SEM; Model 630, FEI, USA), which was operating at 5 kV and a pressure of 0.1–0.5 mbar. The specific surface area of the TMO materials was measured by nitrogen adsorption via the Brauner-Emmet-Teller (BET) technique with a NOVAtouch Surface Area and Pore Size Analyzer (Quantachrome Instruments, USA) operating at 350.5 °C. Samples were degassed under vacuum at 300 °C for 180 min before measurement. Powder X-ray diffraction (pXRD) was performed with an X'pert PRO diffractometer (Malvern PANalytical, UK) equipped with a cobalt source running at 45 kV and 40 mA. The bandgap of the TMO materials was determined from the Tauc plots of the Kubelka-Munk functions of diffuse reflectance spectra (see Supporting Information) collected with a fiber spectrometer (Flame-S-UV–vis-ES, Ocean Optics, USA). Briefly, diffuse reflectance spectra were collected from compacted TMO powders using a reflection probe (QR-400-7-SR). A balanced deuterium tungsten lamp (DH-2000-BAL) was used as the broadband illumination source.

2.8. Sample analysis

A Genesys 10S UV–vis Spectrophotometer (ThermoFisher, USA) was used for spectroscopic analysis. Samples in 1 × 1 × 4.5 cm quartz cuvettes (Starna Cells, Inc.) were scanned from 650 to 200 nm at an interval of 1 nm.

3. Results

3.1. Photocatalyst material characterization

All TMOs were formed as phase pure compounds, as characterized by pXRD (Fig. S3). Commercial TiO_2 (P25) was included as a photocatalytic reference material due to its extensive use in photocatalytic studies [11,20,61–63]. Bandgap information was extrapolated from Tauc plots (Eq. S1, Fig. S4) of diffuse reflectance spectra, and surface area was measured by nitrogen adsorption with the BET technique (Table 1). The morphology of the TMO materials was characterized with an SEM (Fig. 1) and analysis of the images was used to measure the distribution particle lengths (Fig. S5).

Colloids of each TMO composition were formed with homogeneous size and morphology with an average length greater than 200 nm. The individual ZnO particles were anisotropic rods with an average length of 2.2 ± 0.4 μm. The Fe_2O_3 colloids were ellipsoidal with an average length of 0.3 ± 0.1 μm. The CuO materials were formed as spindle-shaped aggregates with an average length of 1.5 ± 0.2 μm. Specific surface area of the particles ranged from a minimum of 3.37 m^2/g for ZnO to a maximum of 26.32 m^2/g for Fe_2O_3, as compared to 53.66 m^2/g for the commercial TiO_2, which corresponds well with literature reports for P25-type TiO_2 [64].

3.2. Photocatalytic performance of individual TMOs

We used MO as a reference contaminant throughout our experiments [65–68], illuminated reactions with a broad-spectrum tungsten system [59], and added H_2O_2 to each experiment as an ROS precursor [49,69–71]. All individual TMO materials degraded MO under broad-spectrum illumination (Figs. S6 and S7). Control experiments with H_2O_2 and light (no particles) did not yield appreciable degradation of MO (Fig. S7). The rate constants for each TMO material varied by a factor of 6 (Table 2), and the percentage of MO degraded after illumination for 60 min ranged from 7% to 78 %.

Overall, the relative ranking of the rate constants (Fe_2O_3 > TiO_2 ~ CuO > ZnO) seems to imply that Fe_2O_3 is the best-performing photocatalyst under these conditions, even though CuO receives a greater incident irradiance (Fig. S2). The photocatalytic rate constants are influenced by the incident light irradiance *and* the surface area of the materials themselves [72,73]. The role of incident irradiance (I_o) was accounted for through calculation of an apparent quantum efficiency (φ_{MO}), as described by Buriak et al. [74]. To better understand the observed trends in the individual TMO experiments, the measured rate constants (k) and the φ_{MO} were normalized to their respective surface areas (SA, Table 2).

The relative rank of the SA normalized rates was CuO > Fe_2O_3 > ZnO > TiO_2, while the φ_{MO} values ranked as TiO_2 > Fe_2O_3 > ZnO > CuO. Moreover, the quantity φ_{MO}/SA ranked as ZnO > TiO_2 > Fe_2O_3 > CuO. These simple calculations illustrate that as a material, CuO performs best on the basis of surface area, while TiO_2 performs the best on the basis of available light (Fig. 1). In terms of the quantity φ_{MO}/SA, ZnO dominates, implying that it yields the highest degradation rate per unit surface area for a given irradiance. Being that ZnO had the lowest overall surface area, this outcome may be a consequence of other factors—for example, the crystallography of the ZnO particles themselves [41,75] or lower recombination rates [70,76]. Overall, these results illustrate the dependence of a material's photocatalytic performance (e.g., photodegradation rate constant) on the surface area as well as the incident irradiance at its absorption wavelength. These results also provide insight into the selection of materials for a given photocatalytic scenario. For example, other factors such as recombination aside, the performance of ZnO may be enhanced by increasing surface area and/or incident irradiance. On the other hand, while the performance of CuO is strongly dependent on surface area, increasing irradiance might not yield increased performance.

3.3. Photocatalytic performance of TMO combinations

Seeking to enhance photocatalytic performance of Fe_2O_3, we made mixtures of TMO colloids using a ternary approach, varying x, y, and z for the general formula $(ZnO)_x(Fe_2O_3)_y(CuO)_z$, where x, y, and z are mole fractions of each TMO. This approach employed the blending rationale used to construct ternary phase diagrams in materials science and ceramic engineering [77] and allowed us to explore the many possible ratios between ZnO, Fe_2O_3, and CuO colloids. For each combination, we performed photocatalytic degradation of MO and used the pseudo-first-order rate constants as a metric to assess the performance enhancement or lack thereof caused by mixing ZnO and CuO colloids with Fe_2O_3. We chose to use the pseudo-first-order rate constants as a metric to allow broader interpretation of the results to other studies.

The ternary plot (Fig. 2a) illustrates one elevated region that spans over the composition range of 0–0.2 ZnO, 0.6–0.8 Fe_2O_3, and 0.15–0.40 CuO. The first-order kinetic-rate data for each point is included in the

Table 1
Pertinent information on transition-metal oxide compounds relevant to this work.

Compound Name	Formula	Bandgap[a] (eV)	Wavelength[b] (nm)	Specific Surface Area[c] (m²/g)	Size, Length[d] (μm)
Zinc oxide (zincite)	ZnO	3.2	388	3.37	2.2 ± 0.4
Iron oxide (hematite)	α-Fe$_2$O$_3$	2.1	590	26.32	0.3 ± 0.1
Copper oxide (tenorite)	CuO	1.7	729	5.94	1.5 ± 0.2
Titanium dioxide (P25)	TiO$_2$	3.3	376	53.66	6.1 ± 0.1[e]

[a] Calculated from diffuse reflectance spectra, Tauc plots included in Fig. S4. All fitting errors were ≤ 0.1 eV.
[b] Converted from calculated bandgap data.
[c] Single point BET, accuracy ± 0.1 % pressure.
[d] Obtained by image analysis of SEM images.
[e] Determined from laser-scattering analysis and does not well represent primary particle sizes due to aggregation.

Supporting Information (Table S1). The highest rate constant for MO degradation was measured for the $x = 0$, $y = 0.7$, $z = 0.3$ combination (0.045(5) min^{-1}), which is at least double the fractional sum of the individual rate constants for Fe$_2$O$_3$ and CuO (0.021 min^{-1}). Similarly high rate constants (0.039(3) and 0.038(2) min^{-1}) were measured for the $x = 0.2$, $y = 0.6$, $z = 0.2$ and the $x = 0$, $y = 0.6$, $z = 0.4$ combinations, which exceed the fractional sum of the individual TMO rate constants (0.016(4), 0.017(4) min^{-1}). It is noteworthy that the rate constant for all combinations was at least double the fractional sum of the individual TMOs, indicating there is an underlying synergy governing the photocatalysis reactions with these TMO combinations. Moreover, only small fractions of ZnO were tolerated in the mixtures; addition of ZnO either decreased the rate constant or had no effect.

The photocatalytic synergy exhibited by the best performing TMO combinations ($x/y/z$ = 0/0.7/0.3, 0.2/0.6/0.2, 0/0.6/0.4, 0/0.8/0.2) is unexpected when experimental aspects are considered. First, all combination experiments were carried out with the same total mass of the TMO catalyst and H$_2$O$_2$. Thus, due to competition for a fixed incident light flux and H$_2$O$_2$ concentration, one might predict that the MO degradation rates for the combination materials would decrease. However, due to the lower surface area of CuO and ZnO as compared to Fe$_2$O$_3$, all the combination reactions had less photocatalyst surface area present in solution than those with Fe$_2$O$_3$ alone (1.0896 m^2, Table 2). Regardless, all these combination experiments had rate constants that were at least double that of Fe$_2$O$_3$ alone, implying that the synergistic increases do not stem from surface area considerations.

A second and unexpected observation was that ZnO only contributes minimally to the rate enhancement. In other words, the observed synergy is largely between Fe$_2$O$_3$ and CuO. For example, consider the 0.2/0.6/0.2 Zn:Fe:Cu compound with a rate constant of 0.039(3) min^{-1}. When the ZnO fraction (0.2) is replaced with CuO, the 0/0.6/0.4 combination material, which has an equivalent rate constant (0.038(2) min^{-1}), is obtained (Table 3, Fig. S8). Conversely, the 0.66/0.34/0 combination material has a rate constant that is reduced to only 32 % (0.012(1) min^{-1}) of the 0/0.6/0.4 material. In other words, ZnO does not appear to be enhancing the rate constant by harvesting additional wavelengths of light; ZnO seems to be inhibiting the photocatalytic performance of Fe$_2$O$_3$. Moreover, combinations of ZnO and CuO alone have rate constants that are an order of magnitude lower in all cases (e.g., 0.75/0/0.25, k = 0.0013 min^{-1}).

Since the performance enhancements were most broadly observed with CuO additions to Fe$_2$O$_3$, a set of experiments with variable masses of Fe$_2$O$_3$ and CuO was performed to further define the compositional range of their synergy. The variable mass experiments (Fig. 2b) identified two maxima in the rate constants for MO degradation: one at 25 mg Fe$_2$O$_3$ and 5 mg CuO (0.045(5) min^{-1}), which is the $x = 0$, $y = 0.7$, $z = 0.3$ combination; and another at 15.0 mg Fe$_2$O$_3$ and 7.5 mg CuO (0.040(1) min^{-1}, Table 3), which has equal mole ratios of Fe$_2$O$_3$ and CuO ($x = 0$, $y = 1.0$, $z = 1.0$). In all cases, the fraction of CuO needed to enhance Fe$_2$O$_3$ photocatalysis was equal to or less than the amount of Fe$_2$O$_3$ present.

The different MO degradation rates for the combination TMO photocatalysts stimulated new questions. First, why does ZnO not enhance the performance of Fe$_2$O$_3$ or CuO? Secondly, what causes the more-than-additive rate constants in the mixed TMO materials? To answer the first question, we had to rule out a few possiblities: that the larger ZnO particles could be i) scattering or ii) blocking light from reaching the other TMO particles or iii) that ZnO with its higher energy bandgap could be absorbing higher energy photons, thereby reducing the irradiance available to excite CuO and Fe$_2$O$_3$. To investigate these possibilities, we performed experiments wherein ZnO was used as a filter for photodegradations with the 0/0.5/0.5 combination by placing a dropcast layer of ZnO onto a quartz disc, which was placed above the reaction beaker during illumination. With this configuration, we measured a rate constant of 0.030(3) min^{-1}. When compared to the 0/0.5/0.5 rate of 0.040(1) min^{-1} and the 0.2/0.6/0.2 rate of 0.039(3) min^{-1}, it is evident that light blocking, scattering, or energy filtering by ZnO is only a minor contributor to the rate decrease measured in the combination experiments. These results suggest that the lack of performance gains with ZnO (first question) and the synergy measured in CuO:Fe$_2$O$_3$ combinations (second question) are related to ROS generation, mainly the possiblity that ZnO may operate with different ROS as compared to
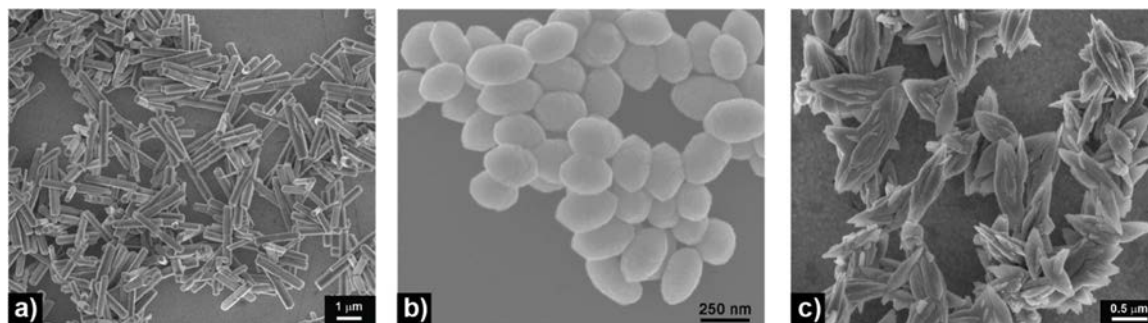

Fig. 1. Morphology of the TMO materials imaged with scanning electron microscopy: (a) ZnO, (b) Fe$_2$O$_3$, and (c) CuO.

Table 2

Properties, rate constants, and metrics of individual TMO photocatalyst experiments for the degradation of MO.

| TMO	Surface Area (SA)[a] (m^2)	Incident Irradiance[b] (I_o) (W/m^2)	Degradation after 60 min. (%)	Rate Constant[c] (k) (min^{-1})	k_{MO}/SA $\left(\frac{1000}{m^2 min}\right)$	$\varphi_{MO}\left(\frac{1000*m^2}{min*W}\right)$	φ_{MO}/SA $\left(\frac{1000}{min*W}\right)$
ZnO	0.101	2.6	7 ± 3	0.001(2)	11.9	0.46	4.57
Fe_2O_3	1.090	31.4	78 ± 10	0.025(6)	22.6	0.78	0.71
CuO	0.178	56.6	24 ± 4	0.005(1)	25.3	0.08	0.45
TiO_2	0.805	1.7	27 ± 2	0.0052(1)	6.45	3.05	3.80

[a] Calculated from specific surface area and actual mass of photocatalyst used in solution.

[b] Integrated from spectral irradiance data over a 50 nm span centered on the relevant wavelength.

[c] All reactions used 30 mg TMO photocatalyst in 40 mL of 25 µM MO. In addition, 100 µL of H_2O_2 (30 %) was added to all TMO experiments except those with TiO_2.
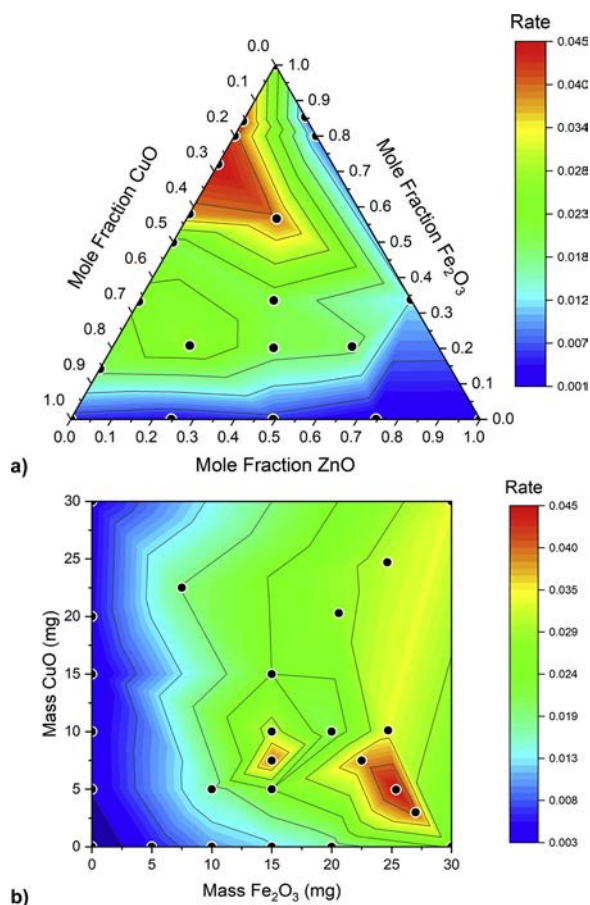
Fig. 2. Contour maps showing pseudo-first-order kinetics for the degradation of MO with mixed phase TMO photocatalytic materials. (*a*) A ternary blend of all three TMO photocatalytic materials used to determine the optimal mole fraction of combination TMO materials. All experiments were conducted with a fixed mass of 30.3(8) mg of photocatalyst. (*b*) Variable mass experiments with various mass ratios of Fe_2O_3-CuO used to find the optimal mass loading for photocatalysis experiments. Two maxima occur: one at 15 mg Fe_2O_3 + 7.5 mg CuO (*x/y/z* = 0/0.5/0.5) and another around 25 mg Fe_2O_3 + 5 mg CuO (*x/y/z* = 0/0.7/0.3). Experiments were conducted in 40 mL of 25 µM MO with 100 µL of H_2O_2 (30 %). A table containing mole frations and rates for each data point are included in the supporting information (Table S1 and S2).

Fe_2O_3 and CuO.

3.4. Mechanism of photocatalytic synergy in mixed TMO compounds

In an effort to understand the enhanced degradation rates in Fe_3O_2-CuO combinations and the limited gains with ZnO, we performed additional experiments adding and removing $HO^{\bullet}$ ROS in the reaction solutions. The addition of H_2O_2 was used to supply an ROS precursor to

Table 3

High performance TMO photocatalyst combinations and their respective rate constants.

ZnO/Fe_2O_3/CuO[a] (mole fraction)	Total Surface Area (SA)[b] (m^2)	Rate Constant[c,d] (k) (min^{-1})
0.2/0.6/0.2	0.465	0.039(3)
0/0.7/0.3	0.688	0.045(5)
0/0.8/0.2	0.736	0.041(3)
0/0.6/0.4	0.632	0.038(2)
0/0.5/0.5[a]	0.439	0.040(1)

[a] All combinations used a total mass of 30 mg in 40 mL of 25 µM MO except the 0/0.5/0.5 formula, which used a total mass of 22.5 mg.

[b] Calculated from specific surface area and the actual mass of photocatalysts used in solution.

[c] Reaction solutions included 100 µL of H_2O_2 (30 %).

[d] Sum of incident irradiance at relevant wavelengths (388, 590, and 729 nm) = 90.6 W/m^2 for the 0.2/0.6/0.2 combination; all other reactions had incident irradiance at relevant wavelengths (590 and 729 nm) = 88.1 W/m^2.

$HO^{\bullet}$ species; the addition of tert-butanol (TBOH) was used to remove $HO^{\bullet}$ species [78].

We first performed serial additions of $HO^{\bullet}$ ROS by adding variable amounts of H_2O_2 to reactions with individual and combination TMOs and monitored the kinetics for MO degradation. Very different dependencies on H_2O_2 were observed for the individual TMO compounds (Fig. 3). For example, the rates for MO degradation by CuO were only
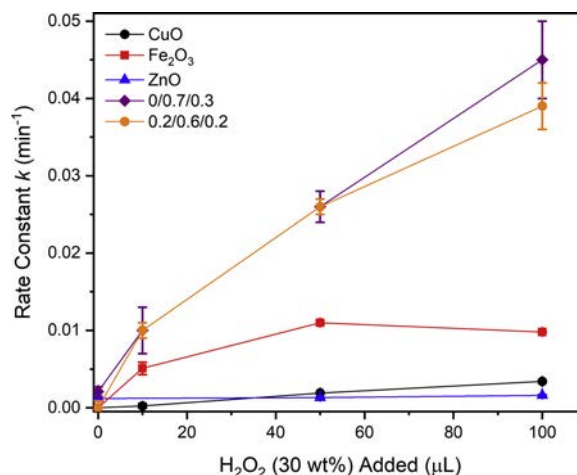
Fig. 3. Experiments performed with serial additions of H_2O_2 as a precursor for $HO^{\bullet}$ ROS. The lack of ZnO dependence on increasing H_2O_2 indicates that ZnO photocatalysis does not strongly depend on $HO^{\bullet}$ ROS. The steep dependence of 0.2/0.6/0.2 and 0/0.7/0.3 combination TMOs on H_2O_2 indicates $HO^{\bullet}$ as the dominant ROS in these reactions. All experiments were performed in 40 mL of 25 µM MO with 30 mg of photocatalyst materials. Illumination was performed for up to 60 min.
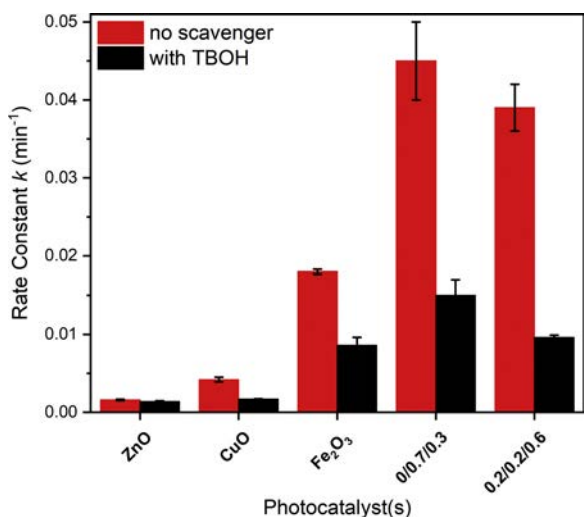
Fig. 4. The observed pseudo-first-order rate constants for experiments with and without TBOH (30 mM) as a scavenger for $HO^{\bullet}$. In the experiments with individual photocatalysts, TBOH decreases the MO degradation rate by over 50 % for CuO and Fe_2O_3 but only by 12 % for ZnO. In both experiments with the combination photocatalytic materials, the presence of TBOH decreases the rate constant by over 75 %. All experiments were performed in 40 mL of 25 μM MO with 30 mg of photocatalyst material. Illumination was performed for up to 60 min. The data table is included in SI (Table S3).

slightly enhanced by the addition of H_2O_2; however, the rate constant of Fe_2O_3 doubled as H_2O_2 was increase from 10 to 50 μL and seemed to saturate by 100 μL. Moreover, the 0.2/0.6/0.2 and 0/0.7/0.3 combination materials both showed a steep dependence on increasing H_2O_2, neither reaching a plateau before 100 μL. Importantly, rate constants for degradation of MO by ZnO showed no dependence on the amount of H_2O_2 in solution. While these results are not a full ROS characterization, they do imply that ZnO-catalyzed photodegradation mechanisms do not rely on H_2O_2, which is a $HO^{\bullet}$ ROS precursor.

Experiments to serially remove $HO^{\bullet}$ ROS from reactions were performed by adding TBOH as an $HO^{\bullet}$ scavenger [78]. Experiments with Fe_2O_3 and CuO alone both exhibited at least a 50 % decrease in rate constant with TBOH in solution (Fig. 4). The 0/0.7/0.3 and 0.2/0.6/0.2 combination materials exhibited a 66 % decrease in the rate constant (from 0.045 to 0.015(2) min^{-1} and from 0.039 to 0.0096(3) min^{-1}, respectively) when $HO^{\bullet}$ were consumed by the presence of TBOH (Figs. 4 and S9). These results indicate not only that CuO and Fe_2O_3 likely rely on $HO^{\bullet}$ as their primary ROS but also that the synergy observed is dependent on the presence of $HO^{\bullet}$ ROS. On the other hand, when $HO^{\bullet}$ are quenched from experiments with ZnO the MO degradation rates are not appreciably affected, leading us to believe that $HO^{\bullet}$ ROS interactions and subsequent quenching in the presence of ZnO [79] govern the CuO/Fe_2O_3 synergy.
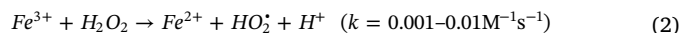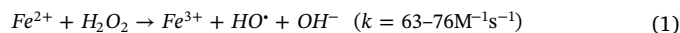
4. Discussion

The photocatalysis reactions carried out with the individual TMOs showed degradation kinetics that were on par with literature reports. Our results for TiO_2 under broad-spectrum light yielded 27 % ± 2% degradation for MO after 1 h. Literature reports on methylene blue (MB) degradation by TiO_2 (P25) under visible and UV illumination have reported 12 % and 25 %, respectively, after 1 h [80]. Our MO photooxidation reactions with ZnO were generally lower than those reported in literature for MB [81] and rhodamine B (RB) [82], likely due to the lower surface-area morphology of our ZnO materials [83]. The Fe_2O_3 materials of this study produced a very similar rate constant as reported for photodegradation of RB with Fe_2O_3 nanostructures [84], MB with Fe_2O_3-kaolin composites [85], and MO with mixed Fe_2O_3 materials

[86]. We measured similar rate constants for MO degradation with CuO as was reported for MB degradation with CuO microspheres [69] and CuO architectures synthesized using bioinspired methods [87].

To date, most research on combination TMO photocatalyts has targeted composite-type materials, where the TMOs are combined as a single material, sharing interfaces with (intimate) nanoscale contact. Such investigations have included CuO-TiO_2 [88,89], Fe_xO_y-TiO_2 [90], and ZnO-CuO [91,92] materials among many others [28,93–96]. As an example, consider that CuO materials decorated with up to 25 % ZnO were reported to have a threefold increase in rate constant over pure CuO alone; the enhancement was attributed to improved charge separation facilitated by ZnO [70]. In contrast, our results indicate that ZnO halts or decreases the rate constant for MO degradation, implying that a different mechanism is at play. In a different report, CuO and ZnO nanoparticles were physically mixed in arsenic-containing solutions, with a maximum in the rate constant at 20 % CuO [97]. Similar to the report above, Samad et al. ascribed their increased rate constant to effective charge transfer between the two oxides, which would enhance charge carrier lifetime as a means to increase the formation of ROS [97].

Since our materials are macroscale mixtures of microscale colloids in solution, where the interactions between the different materials takes place through the aqueous matrix, we suspected that it was ROS interactions in solution that were responsible for the resulting degradation kinetics and not the materials themselves enhancing carrier lifetimes through charge separation. In aqueous solution, metal cations and oxides can activate H_2O_2 to produce $HO^{\bullet}$ through a process that is known as the Fenton (or photo-Fenton if light is applied) reaction [98]. The most classic description of this chemistry involves iron (Eqs. (1) and (2)),

$$Fe^{2+} + H_2O_2 \rightarrow Fe^{3+} + HO^{\bullet} + OH^{-} \quad (k = 63\text{–}76M^{-1}s^{-1}) \tag{1}$$

$$Fe^{3+} + H_2O_2 \rightarrow Fe^{2+} + HO_2^{\bullet} + H^{+} \quad (k = 0.001\text{–}0.01M^{-1}s^{-1}) \tag{2}$$

where applied UV irradiation enhances the $HO^{\bullet}$ yield by reducing Fe^{3+} back to Fe^{2+}. Moreover, in solution with organic dyes the excited state dye can intermolecularly transfer an electron to enhance the Fe^{3+} to Fe^{2+} conversion [98]. Importantly, these reactions can take place heterogeneously on solid iron (oxide) surfaces [99–103]. Other metal surfaces, including copper [104,105], can participate in Fenton-like reactions to produce $HO^{\bullet}$. In contrast, zinc(II) cations are stable (electron configuration $3d^{10}$) and thus do not readily participate in redox (Fenton) reactions. As a result, Fe_2O_3 and CuO photocatalytic reactions are strongly dependent on $HO^{\bullet}$ ROS while ZnO reactions are not.

The $HO^{\bullet}$-addition experiments (Fig. 3) illustrate the dependence of Fe_2O_3 (and CuO to a lesser extent) photoreactions on H_2O_2. In addition, these experiments illustrate a very strong dependence of the Fe_2O_3-CuO combinations on added H_2O_2. Moreover, these experiments revealed an additional feature of the 0/0.7/0.3 Fe_2O_3-CuO combination photocatalyst reactions: a measureable zero-point photodegradation rate (0.002(1) min^{-1}) in the absence of added H_2O_2. This finding implies that the CuO-Fe_2O_3 combination is effective at generating ROS and possibly the ROS precursor H_2O_2.

It is well known that H_2O_2 is activated to $HO^{\bullet}$ by UV light (Eq. (3)) [71]:

$$H_2O_2 + h\nu \overset{\lambda < 300\,nm}{\rightarrow} 2OH^{\bullet} \tag{3}$$

Our illumination source had limited incident UV (Fig. S2) thus the generation of $HO^{\bullet}$ from H_2O_2 is predominantly orchestrated by the oxide photocatalyst materials themselves. Our results indicate that Fe_2O_3 reaction kinetics are strongly dependent on H_2O_2 (Fig. 3) and $HO^{\bullet}$ ROS (Fig. 4). In addition, CuO has been reported to produce H_2O_2 via two-electron reduction in water (Eq. (4)) [106] and to decompose H_2O_2 in the absence of light (Eq. (1)) [39,107]:

$$Cu^{2+} + 2HO_2 \rightarrow Cu^0 + H_2O_2 + 2H^{+} \tag{4}$$

6
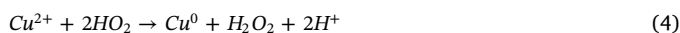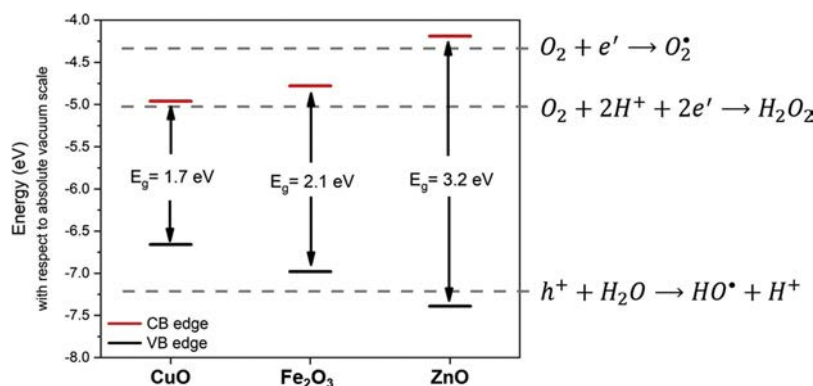
Fig. 5. Schematic illustration of the relative energy levels associated with each of the TMO photocatalysts and the related ROS probed in this study. $HO^\bullet$ generation is within the valence-band (VB) energy for both Fe_2O_3 and CuO but above the VB of ZnO. Conversely, $O_2^{\bullet-}$ formation energy is energetically downhill from the ZnO conduction band (CB) but well above the CB edges of Fe_2O_3 and CuO. These redox and band edge energies rationalize how ZnO photocatalysis operates on different ROS than Fe_2O_3 and CuO.

In the context of these previous reports, our results describe a scenario wherein the synergistic effects present in the 0/0.7/0.3 combination arise from reactions between the TMOs and H_2O_2 in solution. Specifically, we posit that CuO plays a supportive role to Fe_2O_3 photocatalysis by decomposing H_2O_2 to generate $HO^\bullet$ ROS. With additional ROS available, the Fe_2O_2 reaction kinetics are enhanced without a required increase in the incident irradiance or Fe_2O_3 surface area.

The bandgap energies of the TMOs used in this study further corroborate the redox chemistry above. Smaller bandgap materials, such as Fe_2O_3 and CuO, have valence-band edges that are greater than the oxidation potential of H_2O (Fig. 5). As a result, it is energetically favorable for a photogenerated hole (h^+) on Fe_2O_3 or CuO to participate in $HO^\bullet$ generation by H_2O oxidation. Larger bandgap materials, such as ZnO, have valence-band edges that are below the H_2O oxidation potential for $HO^\bullet$ formation, but their conduction band edges are below the reduction potential for O_2. This means that it is energetically favorable for the photogenerated electron from ZnO to participate in O_2 reduction to generate non- $HO^\bullet$ ROS (e.g., $O_2^{\bullet-}$). In a system containing both types of materials (wide and small bandgap), the two processes conflict. For example, H_2O_2 can be reduced to water by $O_2^{\bullet-}$ ROS [18,19] thereby quenching $HO^\bullet$ sources (e.g., H_2O_2) from solution to decrease the photodegradation rate constants. In the context of our results, these interactions describe a consistent scenario wherein ROS interactions can be leveraged to enhance photocatalytic degradation of contaminants in water. In particular, mixed compounds with similar ROS chemistries can yield gains that exceed the sum of their parts.

5. Conclusions

By combining TMO photocatalysts (ZnO, Fe_2O_3, and CuO) with different bandgap energies, we were able to enhance the photocatalytic performance of Fe_2O_3 for removal of MO from aqueous solutions. While all three TMOs are capable of harvesting wavelengths of light from different regions of the solar spectrum, it was predominantly Fe_2O_3-CuO combinations that had enhanced performance. The negative effect of combining Fe_2O_3 (as well as CuO) with ZnO provided insight into the mechanism governing the Fe_2O_3-CuO synergy. This synergy, which is related to more than just increased light harvesting by multiple oxides, results from mechanisms that involve ROS interactions, in particular, a like identity between the ROS in each of the TMOs. Thus the degradation kinetics of the Fe_2O_3-CuO combination materials, where both oxides predominantly operate with $HO^\bullet$ ROS, are not enhanced by the addition of ZnO, which was found to have ROS mechanisms that do not depend on $HO^\bullet$ ROS. We identified a mechanism that is consistent with compatible pairing of ROS and heterogeneous photo-Fenton chemistries. These findings provide a fundamental design methodology to achieve high photocatalytic performance in low-cost, earth-abundant materials based on their bandgap energies and their relation to ROS energies. This approach may open new pathways to enhance photocatalytic removal of small molecule contaminants from water beyond only niche applications.

Author contributions

The manuscript was written through contributions of all authors. EKA and EB performed experiments and analysis; EA-S and JAB performed data analysis and assimilation; EA-S lead in writing. All authors have given approval to the final version of the manuscript.

CRediT authorship contribution statement

Emily Asenath-Smith: Conceptualization, Formal analysis, Investigation, Methodology, Supervision, Project administration, Visualization, Writing - original draft, Writing - review & editing. **Emma K. Ambrogi:** Data curation, Formal analysis, Writing - original draft. **Eftihia Barnes:** Data curation, Formal analysis, Writing - review & editing. **Jonathon A. Brame:** Conceptualization, Formal analysis, Funding acquisition, Methodology, Project administration, Writing - review & editing.

Appendix A. Supplementary data

Supplementary material related to this article can be found in the online version at: https://doi.org/10.1016/j.colsurfa.2020.125179.

References

[1] E.T. Furlong, et al., Nationwide reconnaissance of contaminants of emerging concern in source and treated drinking waters of the United States: pharmaceuticals, Sci. Total Environ. 579 (2017) 1629–1642.

[2] S. Ahmed, M.G. Rasul, R. Brown, M.A. Hashib, Influence of parameters on the heterogeneous photocatalytic degradation of pesticides and phenolic contaminants in wastewater: a short review, J. Environ. Manage. 92 (2011) 311–330, https://doi.org/10.1016/j.jenvman.2010.08.028.

[3] R. Andreozzi, M. Raffaele, P. Nicklas, Pharmaceuticals in STP effluents and their solar photodegradation in aquatic environment, Chemosphere 50 (2003) 1319–1330, https://doi.org/10.1016/s0045-6535(02)00769-5.

[4] N. Le-Minh, S.J. Khan, J.E. Drewes, R.M. Stuetz, Fate of antibiotics during municipal water recycling treatment processes, Water Res. 44 (2010) 4295–4323, https://doi.org/10.1016/j.watres.2010.06.020.

[5] A.M. Gorito, A.R. Ribeiro, C.R. Gomes, C.M.R. Almeida, A.M.T. Silva, Constructed wetland microcosms for the removal of organic micropollutants from freshwater aquaculture effluents, Sci. Total Environ. 644 (2018) 1171–1180, https://doi.org/10.1016/j.scitotenv.2018.06.371.

[6] S. Jiménez, M. Micó, M. Arnaldos, F. Medina, S. Contreras, State of the art of produced water treatment, Chemosphere 192 (2018) 186–208.

[7] T.A. Ternes, J. Adriano, Hansruedi Siegrist, Scrutinizing pharmaceuticals and personal care products in wastewater treatment, Environ. Sci. Technol. (2004) 394A–399A.

[8] V.K. Gupta, I. Ali, T.A. Saleh, A. Nayak, S. Agarwal, Chemical treatment technologies for waste-water recycling—an overview, RSC Adv. 2 (2012) 6380, https://doi.org/10.1039/c2ra20340e.

[9] K.C. Kabra, Sawheny Rubina, L. Rameshwar, Treatment of hazardous organic and inorganic compounds through aqueous-phase photocatalysis: a review, Ind. Eng. Chem. Res. 43 (2004) 7683–7696.

[10] D.M. Robert, Sixto, Solar photocatalysis: a clean process for water detoxification, Sci. Total Environ. 219 (2002) 85–97.

[11] S.K. Loeb, et al., The technology horizon for photocatalytic water treatment: sunrise or sunset? Environ. Sci. Technol. 53 (6) (2018) 2937–2947, https://doi.org/10.1021/acs.est.8b05041.

[12] S. Kwon, M. Fan, A.T. Cooper, H. Yang, Photocatalytic applications of micro- and nano-TiO2 in environmental engineering, Crit. Rev. Environ. Sci. Technol. 38 (2008) 197–226, https://doi.org/10.1080/10643380701628933.

[13] J. Schneider, et al., Understanding TiO2 photocatalysis: mechanisms and materials, Chem. Rev. 114 (2014) 9919–9986, https://doi.org/10.1021/cr5001892.

[14] R. Lei, et al., Hydrothermal synthesis of CdS nanorods anchored on alpha-Fe2O3 nanotube arrays with enhanced visible-light-driven photocatalytic properties, J. Colloid Interface Sci. 514 (2018) 496–506, https://doi.org/10.1016/j.jcis.2017.12.061.

[15] H. Sun, et al., Zinc oxide/vanadium pentoxide heterostructures with enhanced day-night antibacterial activities, J. Colloid Interface Sci. 547 (2019) 40–49, https://doi.org/10.1016/j.jcis.2019.03.061.

[16] H. De Lasa, B. Serrano, M. Salaices, Photocatalytic Reaction Engineering, Springer Science and Business Media, 2005.

[17] M. Pelaez, et al., A review on the visible light active titanium dioxide photocatalysts for environmental applications, Appl. Catal. B-Environ. 125 (2012) 331–349.

[18] Y.N. Nosaka, Y. Atsuko, Pierre Pichat (Ed.), Photocatalysis and Water Purification: From Fundamentals to Recent Applications, Wiley VCH, 2013, pp. 3–24 Ch. 1.

[19] T. Hirakawa, Y. Nosaka, Selective production of superoxide ions and hydrogen peroxide over nitrogen-and sulfur-doped TiO2 photocatalysts with visible light in aqueous suspension systems, J. Phys. Chem. C 112 (2008) 15818–15823.

[20] J. Lee, C-60 aminofullerene immobilized on silica as a visible-light-activated photocatalyst, Environ. Sci. Technol. 44 (2010) 9488–9495, https://doi.org/10.1021/es1028475.

[21] S.G. Kumar, L.G. Devi, Review on modified TiO2 photocatalysis under UV/visible light: selected results and related mechanisms on interfacial charge carrier transfer dynamics, J. Phys. Chem. A 115 (2011) 13211–13241, https://doi.org/10.1021/jp204364a.

[22] X. Yan, et al., The interplay of sulfur doping and surface hydroxyl in band gap engineering: mesoporous sulfur-doped TiO2 coupled with magnetite as a recyclable, efficient, visible light active photocatalyst for water purification, Appl. Catal. B-Environ. 218 (2017) 20–31, https://doi.org/10.1016/j.apcatb.2017.06.022.

[23] J.Z. Bloh, R. Dillert, D.W. Bahnemann, Designing optimal metal-doped photocatalysts: correlation between photocatalytic activity, doping ratio, and particle size, J. Phys. Chem. C 116 (2012) 25558–25562, https://doi.org/10.1021/jp307313z.

[24] M. Nasr, C. Eid, R. Habchi, P. Miele, M. Bechelany, Recent progress on titanium dioxide nanomaterials for photocatalytic applications, Chemsuschem 11 (2018) 3023–3047, https://doi.org/10.1002/cssc.201800874.

[25] L.V. Bora, R.K. Mewada, Visible/solar light active photocatalysts for organic effluent treatment: fundamentals, mechanisms and parametric review, Renew. Sustain. Energy Rev. 76 (2017) 1393–1421, https://doi.org/10.1016/j.rser.2017.01.130.

[26] M. Nolan, A. Iwaszuk, A.K. Lucid, J.J. Carey, M. Fronzi, Design of novel visible light active photocatalyst materials: surface modified TiO2, Adv. Mater. 28 (2016) 5425–5446, https://doi.org/10.1002/adma.201504894.

[27] M.G. Méndez-Medrano, et al., Surface modification of TiO2 with Ag nanoparticles and CuO nanoclusters for application in photocatalysis, J. Phys. Chem. C 120 (2016) 5143–5154, https://doi.org/10.1021/acs.jpcc.5b10703.

[28] W. Yan, H. Fan, C. Yang, Ultra-fast synthesis and enhanced photocatalytic properties of alpha-Fe2O3/ZnO core-shell structure, Mater. Lett. 65 (2011) 1595–1597.

[29] J. Yu, G. Dai, B. Huang, Fabrication and characterization of visible-light-driven plasmonic photocatalyst Ag/AgCl/TiO2 TiO2 nanotube arrays, J. Phys. Chem. C 113 (2009) 16394–16401, https://doi.org/10.1021/jp905247j.

[30] E. Asenath-Smith, et al., Physical confinement promoting formation of Cu2O–Au heterostructures with Au nanoparticles entrapped within crystalline Cu2O nanorods, Chem. Mater. 29 (2016) 555–563.

[31] Y. Choi, et al., Sequential process combination of photocatalytic oxidation and dark reduction for the removal of organic pollutants and Cr (VI) using Ag/TiO2, Environ. Sci. Technol. 51 (2017) 3973–3981.

[32] F.J. Heiligtag, et al., Self-assembly of metal and metal oxide nanoparticles and nanowires into a macroscopic ternary aerogel monolith with tailored photocatalytic properties, Chem. Mater. 26 (2014) 5576–5584, https://doi.org/10.1021/cm502063f.

[33] R. Ghosh Chaudhuri, S. Paria, Core/shell nanoparticles: classes, properties, synthesis mechanisms, characterization, and applications, Chem. Rev. 112 (2012) 2373–2433, https://doi.org/10.1021/cr100449n.

[34] Q.Q. Yin, et al., Glucose-assisted transformation of Ni-doped-ZnO@carbon to a Ni-doped-ZnO@void@SiO2 core-shell nanocomposite photocatalyst, RSC Adv. 6 (2016) 38653–38661, https://doi.org/10.1039/c5ra26631a.

[35] X.H. Zhang, et al., A bamboo-inspired hierarchical nanoarchitecture of Ag/CuO/TiO2 nanotube array for highly photocatalytic degradation of 2,4-dinitrophenol, J. Hazard. Mater. 313 (2016) 244–252, https://doi.org/10.1016/j.jhazmat.2016.03.094.

[36] H. Saito, Y. Nosaka, Mechanism of singlet oxygen generation in visible-light-induced photocatalysis of gold-nanoparticle-deposited titanium dioxide, J. Phys. Chem. C 118 (2014) 15656–15663.

[37] A. Kay, I. Cesar, M. Grätzel, New benchmark for water photooxidation by nanostructured α-Fe2O3 films, J. Am. Chem. Soc. 128 (2006) 15714–15721, https://doi.org/10.1021/ja064380l.

[38] H.G. Cha, S.J. Kim, K.J. Lee, M.H. Jung, Y.S. Kang, Single-crystalline porous hematite nanorods: photocatalytic and magnetic properties, J. Phys. Chem. C 115 (2011) 19129–19135.

[39] H. Zhou, S.S. Wong, A facile and mild synthesis of 1-D ZnO, CuO, and α-Fe2O3 nanostructures and nanostructured arrays, ACS Nano 2 (2008) 944–958.

[40] S.C. Warren, et al., Identifying champion nanostructures for solar water-splitting, Nat. Mater. 12 (2013) 842–849, https://doi.org/10.1038/nmat3684.

[41] E. Asenath-Smith, R. Hovden, L.F. Kourkoutis, L.A. Estroff, Hierarchically structured hematite architectures achieved by growth in a silica hydrogel, J. Am. Chem. Soc. 137 (2015) 5184–5192, https://doi.org/10.1021/jacs.5b01697.

[42] H. Wu, T. Yang, Y.H. Du, L. Shen, G.W. Ho, Identification of facet-governing reactivity in hematite for oxygen evolution, Adv. Mater. 30 (2018), https://doi.org/10.1002/adma.201804341.

[43] X. Huang, et al., Flower-like porous hematite nanoarchitectures achieved by complexation-mediated oxidation-hydrolysis reaction, J. Colloid Interface Sci. 357 (2011) 36–45, https://doi.org/10.1016/j.jcis.2011.02.001.

[44] X.J. Liu, J.F. Liu, Z. Chang, X.M. Sun, Y.D. Li, Crystal plane effect of Fe2O3 with various morphologies on CO catalytic oxidation, Catal. Commun. 12 (2011) 530–534, https://doi.org/10.1016/j.catcom.2010.11.016.

[45] F. Baig, Y.H. Khattak, S. Jemai, B.M. Soucase, S. Beg, Hydrothermal syntheses of Vanadium doped alpha - Fe2O3 cubic particles with enhanced photoelectrochemical activity, Sol. Energy 182 (2019) 332–339, https://doi.org/10.1016/j.solener.2019.02.066.

[46] X.M. Zhou, et al., Visible light induced photocatalytic degradation rhodamine B on one-dimensional Iron oxide particles, J. Phys. Chem. C 114 (2010) 17051–17061, https://doi.org/10.1021/jp103816e.

[47] F. Lu, W. Cai, Y. Zhang, ZnO hierarchical micro/nanoarchitectures: solvothermal synthesis and structurally enhanced photocatalytic performance, Adv. Funct. Mater. 18 (2008) 1047–1056.

[48] S. Ma, R. Li, C. Lv, W. Xu, X. Gou, Facile synthesis of ZnO nanorod arrays and hierarchical nanostructures for photocatalysis and gas sensor applications, J. Hazard. Mater. 192 (2011) 730–740.

[49] J.P. Li, et al., Preparation of spindly CuO micro-particles for photodegradation of dye pollutants under a halogen tungsten lamp, Appl. Catal. A-Gen. 406 (2011) 51–58, https://doi.org/10.1016/j.apcata.2011.08.007.

[50] B. Shaabani, E. Alizadeh-Gheshlaghi, Y. Azizian-Kalandaragh, A. Khodayari, Preparation of CuO nanopowders and their catalytic activity in photodegradation of Rhodamine-B, Adv. Powder Technol. 25 (2014) 1043–1052.

[51] J. Lee, S. Zhang, S. Sun, High-temperature solution-phase syntheses of metal-oxide nanocrystals, Chem. Mater. 25 (2013) 1293–1304, https://doi.org/10.1021/cm3040517.

[52] M. Vaseem, A. Umar, S.H. Kim, Y.B. Hahn, Low-temperature synthesis of flower-shaped CuO nanostructures by solution process: formation mechanism and structural properties, J. Phys. Chem. C 112 (2008) 5729–5735, https://doi.org/10.1021/jp710358j.

[53] C. Frandsen, et al., Aggregation-induced growth and transformation of β-FeOOH nanorods to micron-sized α-Fe2O3 spindles, CrystEngComm 16 (2014) 1451–1458.

[54] R. Muñoz-Espí, Y. Qi, I. Lieberwirth, C.M. Gomez, G. Wegner, Surface-functionalized latex particles as controlling agents for the mineralization of zinc oxide in aqueous medium, Chem. Eur. J. 12 (2006) 118–129.

[55] R. Munoz-Espi, C. Amreesh, G. Wegner, Crystal perfection in zinc oxide with occluded carboxyl-functionalized latex particles, Cryst. Growth Des. 7 (2007)

1584–1589.

[56] C. Frandsen, et al., Aggregation-induced growth and transformation of β-FeOOH nanorods to micron-sized α-Fe2O3spindles, CrystEngComm 16 (2014) 1451–1458, https://doi.org/10.1039/c3ce40983j.

[57] J. Li, et al., Preparation of spindly CuO micro-particles for photodegradation of dye pollutants under a halogen tungsten lamp, Appl. Catal. A Gen. 406 (2011) 51–58, https://doi.org/10.1016/j.apcata.2011.08.007.

[58] M. Vaseem, A. Umar, S.H. Kim, Y.-B. Hahn, Low-temperature synthesis of flower-shaped CuO nanostructures by solution process: formation mechanism and structural properties, J. Phys. Chem. C 112 (2008) 5729–5735, https://doi.org/10.1021/jp710358j.

[59] E. Asenath-Smith, E.K. Ambrogi, L.C. Moores, S.D. Newman, J.A. Brame, Leveraging chemical actinometry and optical radiometry to reduce uncertainty in photochemical research, J. Photochem. Photobiol. A: Chem. 372 (2019) 279–287, https://doi.org/10.1016/j.jphotochem.2018.12.024.

[60] Y. Liao, et al., Photocatalytic generation of multiple ROS types using low-temperature crystallized anodic TiO2 nanotube arrays, J. Hazard. Mater. 260 (2013) 434–441.

[61] F. Piccinno, F. Gottschalk, S. Seeger, B. Nowack, Industrial production quantities and uses of ten engineered nanomaterials in Europe and the world, J. Nanoparticle Res. 14 (1109) (2012).

[62] Y.L. Liao, et al., Photocatalytic generation of multiple ROS types using low-temperature crystallized anodic TiO2 nanotube arrays, J. Hazard. Mater. 260 (2013) 434–441, https://doi.org/10.1016/j.jhazmat.2013.05.047.

[63] C. Chen, et al., Photocatalysis by titanium dioxide and polyoxometalate/TiO2 cocatalysts. Intermediates and mechanistic study, Environ. Sci. Technol. 38 (2004) 329–337.

[64] K. Suttiponparnit, et al., Role of surface area, primary particle size, and crystal phase on titanium dioxide nanoparticle dispersion properties, Nanoscale Res. Lett. 6 (2011) 27.

[65] B. Qiu, M. Xing, J. Zhang, Mesoporous TiO2 nanocrystals grown in situ on graphene aerogels for high photocatalysis and lithium-ion batteries, J. Am. Chem. Soc. 136 (2014) 5852–5855, https://doi.org/10.1021/ja500873u.

[66] R. Wakimoto, T. Kitamura, F. Ito, H. Usami, H. Moriwaki, Decomposition of methyl orange using C60 fullerene adsorbed on silica gel as a photocatalyst via visible-light induced electron transfer, Appl. Catal. B-Environ. 166–167 (2015) 544–550, https://doi.org/10.1016/j.apcatb.2014.12.010.

[67] L. Zhou, J. Lei, L. Wang, Y. Liu, J. Zhang, Highly efficient photo-Fenton degradation of methyl orange facilitated by slow light effect and hierarchical porous structure of Fe2O3-SiO2 photonic crystals, Appl. Catal. B-Environ. 237 (2018) 1160–1167, https://doi.org/10.1016/j.apcatb.2017.08.039.

[68] S.C. Yan, Z.S. Li, Z.G. Zou, Photodegradation of rhodamine B and methyl orange over boron-doped g-C3N4 under visible light irradiation, Langmuir 26 (2010) 3894–3901, https://doi.org/10.1021/la904023j.

[69] M. Rabbani, R. Rahimi, M. Bozorgpour, J. Shokraiyan, S.S. Moghaddam, Photocatalytic application of hollow CuO microspheres with hierarchical dandelion-like structures synthesized by a simple template free approach, Mater. Lett. 119 (2014) 39–42, https://doi.org/10.1016/j.matlet.2013.12.095.

[70] K. Mageshwari, D. Nataraj, T. Pal, R. Sathyamoorthy, J. Park, Improved photocatalytic activity of ZnO coupled CuO nanocomposites synthesized by reflux condensation method, J. Alloys Compd. 625 (2015) 362–370.

[71] F. Banat, S. Al-Asheh, M. Nusair, Photodegradation of methylene blue dye by the UV/H2O2 and UV/acetone oxidation processes, Desalination 181 (2005) 225–232.

[72] J.R. Bolton, I. Mayor-Smith, K.G. Linden, Rethinking the concepts of fluence (UV dose) and fluence rate: the importance of photon-based units–a systemic review, Photochem. Photobiol. 91 (2015) 1252–1262.

[73] T. Tachikawa, T. Majima, Single-molecule fluorescence imaging of TiO2 photocatalytic reactions, Langmuir 25 (2009) 7791–7802.

[74] J.M. Buriak, P.V. Kamat, K.S. Schanze (ACS Publications, 2014).

[75] H.F. Greer, W. Zhou, M.-H. Liu, Y.-H. Tseng, C.-Y. Mou, The origin of ZnO twin crystals in bio-inspired synthesis, CrystEngComm 14 (2012) 1247–1255.

[76] M. Quintana, T. Edvinsson, A. Hagfeldt, G. Boschloo, Comparison of dye-sensitized ZnO and TiO2 solar cells: studies of charge transport and carrier lifetime, J. Phys. Chem. C 111 (2007) 1035–1041.

[77] D.R.F. West, Ternary Phase Diagrams in Materials Science, Routledge, 2017.

[78] G.P. Anipsitakis, D.D. Dionysiou, Radical generation by the interaction of transition metals with common oxidants, Environ. Sci. Technol. 38 (2004) 3705–3712.

[79] Q. Xiang, J. Yu, P.K. Wong, Quantitative characterization of hydroxyl radicals produced by various photocatalysts, J. Colloid Interface Sci. 357 (2011) 163–167.

[80] H. Zhang, X. Lv, Y. Li, Y. Wang, J. Li, P25-graphene composite as a high performance photocatalyst, ACS Nano 4 (2010) 380–386.

[81] I. Fatimah, S. Wang, D. Wulandari, ZnO/montmorillonite for photocatalytic and photochemical degradation of methylene blue, Appl. Clay Sci. 53 (2011) 553–560.

[82] Y. Miao, H. Zhang, S. Yuan, Z. Jiao, X. Zhu, Preparation of flower-like ZnO architectures assembled with nanosheets for enhanced photocatalytic activity, J.

Colloid Interface Sci. 462 (2016) 9–18.

[83] E. Topkaya, M. Konyar, H.C. Yatmaz, K. Öztürk, Pure ZnO and composite ZnO/TiO2 catalyst plates: a comparative study for the degradation of azo dye, pesticide and antibiotic in aqueous solutions, J. Colloid Interface Sci. 430 (2014) 6–11.

[84] A. Kusior, K. Michalec, P. Jelen, M. Radecka, Shaped Fe2O3 nanoparticles–synthesis and enhanced photocatalytic degradation towards RhB, Appl. Surf. Sci. 476 (2019) 342–352.

[85] S. Guo, G. Zhang, J. Wang, Photo-Fenton degradation of rhodamine B using Fe2O3–Kaolin as heterogeneous catalyst: characterization, process optimization and mechanism, J. Colloid Interface Sci. 433 (2014) 1–8.

[86] C. Jaramillo-Páez, J.A. Navío, M. Hidalgo, A. Bouziani, M. El Azzouzi, Mixed α-Fe2O3/Bi2WO6 oxides for photoassisted hetero-Fenton degradation of Methyl Orange and Phenol, J. Photochem. Photobiol. A: Chem. 332 (2017) 521–533.

[87] M.A. Prathap, B. Kaur, R. Srivastava, Hydrothermal synthesis of CuO micro-/nanostructures and their applications in the oxidative degradation of methylene blue and non-enzymatic sensing of glucose/H2O2, J. Colloid Interface Sci. 370 (2012) 144–154.

[88] G. Li, N.M. Dimitrijevic, L. Chen, T. Rajh, K.A. Gray, Role of surface/interfacial Cu2+ sites in the photocatalytic activity of coupled CuO − TiO2 nanocomposites, J. Phys. Chem. C 112 (2008) 19040–19044.

[89] Z. Jin, X. Zhang, Y. Li, S. Li, G. Lu, 5.1% Apparent quantum efficiency for stable hydrogen generation over eosin-sensitized CuO/TiO2 photocatalyst under visible light irradiation, Catal. Commun. 8 (2007) 1267–1273.

[90] J.A. Libera, J.W. Elam, N.F. Sather, T. Rajh, N.M. Dimitrijevic, Iron(III)-oxo centers on TiO2 for visible-light photocatalysis, Chem. Mater. 22 (2010) 409–413, https://doi.org/10.1021/cm902825c.

[91] S. Das, V.C. Srivastava, Hierarchical nanostructured ZnO-CuO nanocomposite and its photocatalytic activity, J. Nano Res. 35 (2016) 21–26, https://doi.org/10.4028/www.scientific.net/JNanoR.35.21.

[92] R. Saravanan, et al., Enhanced photocatalytic activity of ZnO/CuO nanocomposite for the degradation of textile dye on visible light illumination, Mater. Sci. Eng. C 33 (2013) 91–98.

[93] R. Li, L. Yu, X. Yan, Q. Tang, Efficient photocatalysts from polymorphic cuprous oxide/zinc oxide microstructures, RSC Adv. 5 (2015) 11917–11924.

[94] R. Michal, et al., Photocatalytic properties and selective antimicrobial activity of TiO2 (Eu)/CuO nanocomposite, Appl. Surf. Sci. 371 (2016) 538–546.

[95] J. Mani, H. Sakeek, S. Habouti, M. Dietze, M. Es-Souni, Macro–meso-porous TiO 2, ZnO and ZnO–TiO 2-composite thick films. Properties and application to photocatalysis, Catal. Sci. Technol. 2 (2012) 379–385.

[96] L. Zhu, et al., Designing 3D-MoS2 sponge as excellent cocatalysts in advanced oxidation processes for pollutant control, Angew. Chem. Int. Ed. 59 (2020) 2–11, https://doi.org/10.1002/anie.202006059.

[97] A. Samad, M. Furukawa, H. Katsumata, T. Suzuki, S. Kaneco, Photocatalytic oxidation and simultaneous removal of arsenite with CuO/ZnO photocatalyst, J. Photochem. Photobiol. A-Chem. 325 (2016) 97–103, https://doi.org/10.1016/j.jphotochem.2016.03.035.

[98] A.D. Bokare, W. Choi, Review of iron-free Fenton-like systems for activating H2O2 in advanced oxidation processes, J. Hazard. Mater. 275 (2014) 121–135.

[99] Y. Zhang, J. He, R. Shi, P. Yang, Preparation and photo Fenton-like activities of high crystalline CuO fibers, Appl. Surf. Sci. 422 (2017) 1042–1051.

[100] J. Herney-Ramirez, M.A. Vicente, L.M. Madeira, Heterogeneous photo-Fenton oxidation with pillared clay-based catalysts for wastewater treatment: a review, Appl. Catal. B-Environ. 98 (2010) 10–26, https://doi.org/10.1016/j.apcatb.2010.05.004.

[101] S.R. Pouran, A.A. Aziz, W.M.A.W. Daud, Review on the main advances in photo-Fenton oxidation system for recalcitrant wastewaters, J. Ind. Eng. Chem. 21 (2015) 53–69.

[102] P. Nidheesh, Heterogeneous Fenton catalysts for the abatement of organic pollutants from aqueous solution: a review, RSC Adv. 5 (2015) 40552–40577.

[103] P. Avetta, et al., Activation of persulfate by irradiated magnetite: implications for the degradation of phenol under heterogeneous photo-Fenton-like conditions, Environ. Sci. Technol. 49 (2015) 1043–1050.

[104] S. Wang, Q. Li, F. Chen, J. Ke, R. Chen, HEPES-mediated controllable synthesis of hierarchical CuO nanostructures and their analogous photo-Fenton and antibacterial performance, Adv. Powder Technol. 28 (2017) 1332–1339.

[105] H.-J. Lee, H. Lee, C. Lee, Degradation of diclofenac and carbamazepine by the copper (II)-catalyzed dark and photo-assisted Fenton-like systems, Chem. Eng. J. 245 (2014) 258–264.

[106] Y. Nosaka, S. Takahashi, H. Sakamoto, A.Y. Nosaka, Reaction mechanism of Cu (II)-grafted visible-light responsive TiO2 and WO3 photocatalysts studied by means of ESR spectroscopy and chemiluminescence photometry, J. Phys. Chem. C 115 (2011) 21283–21290.

[107] D. Drijvers, H. Van Langenhove, M. Beckers, Decomposition of phenol and trichloroethylene by the ultrasound/H2O2/CuO process, Water Res. 33 (1999) 1187–1194.

SUPPORTING INFORMATION

PHOTOCATALYSIS EXPERIMENTAL SETUP:
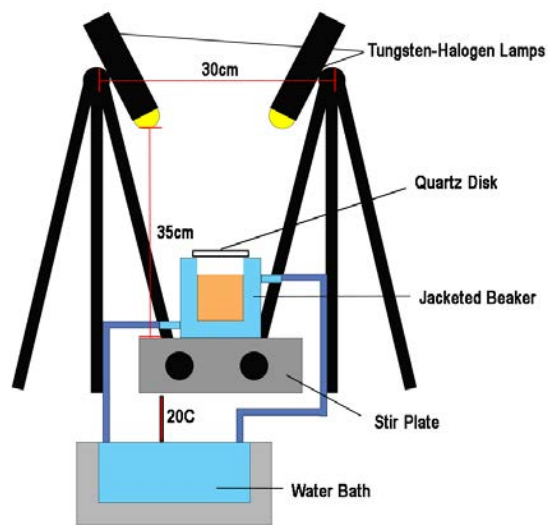
Figure S1. Graphical illustration of the experimental setup used to perform full-spectrum illumination to photocatalysis experiments performed in the laboratory.
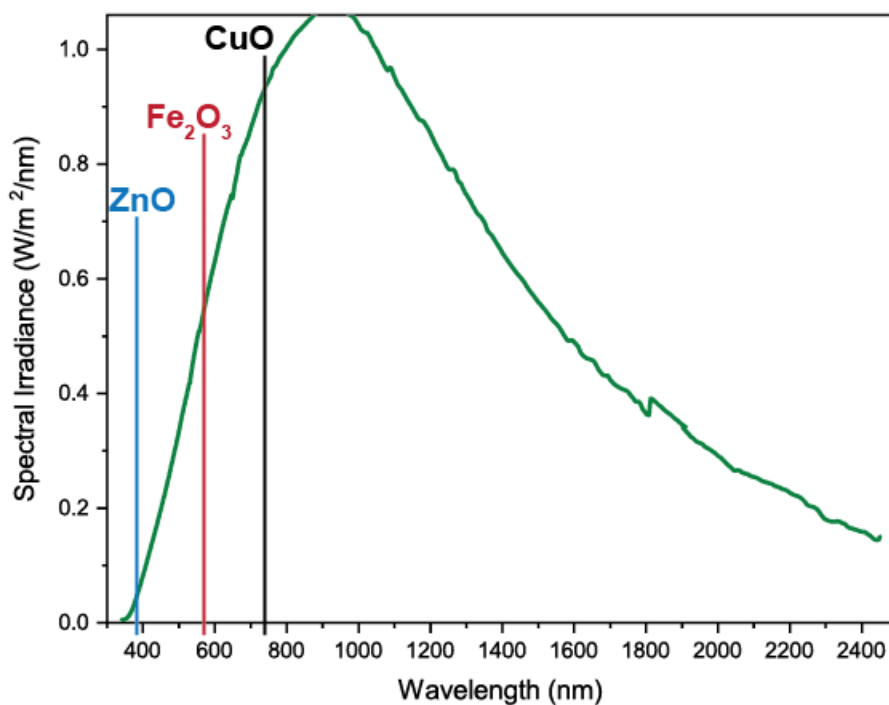
Figure S2. Spectral irradiance of the tungsten halogen illumination system used for photocatalysis experiments. The response wavelengths of each of the transition metal oxide photocatalysts is included. See also Table 1. Note the illumination system is based on two 50 Watt tungsten halogen bulbs.

PHOTOCATALYST CHARACTERIZATION:
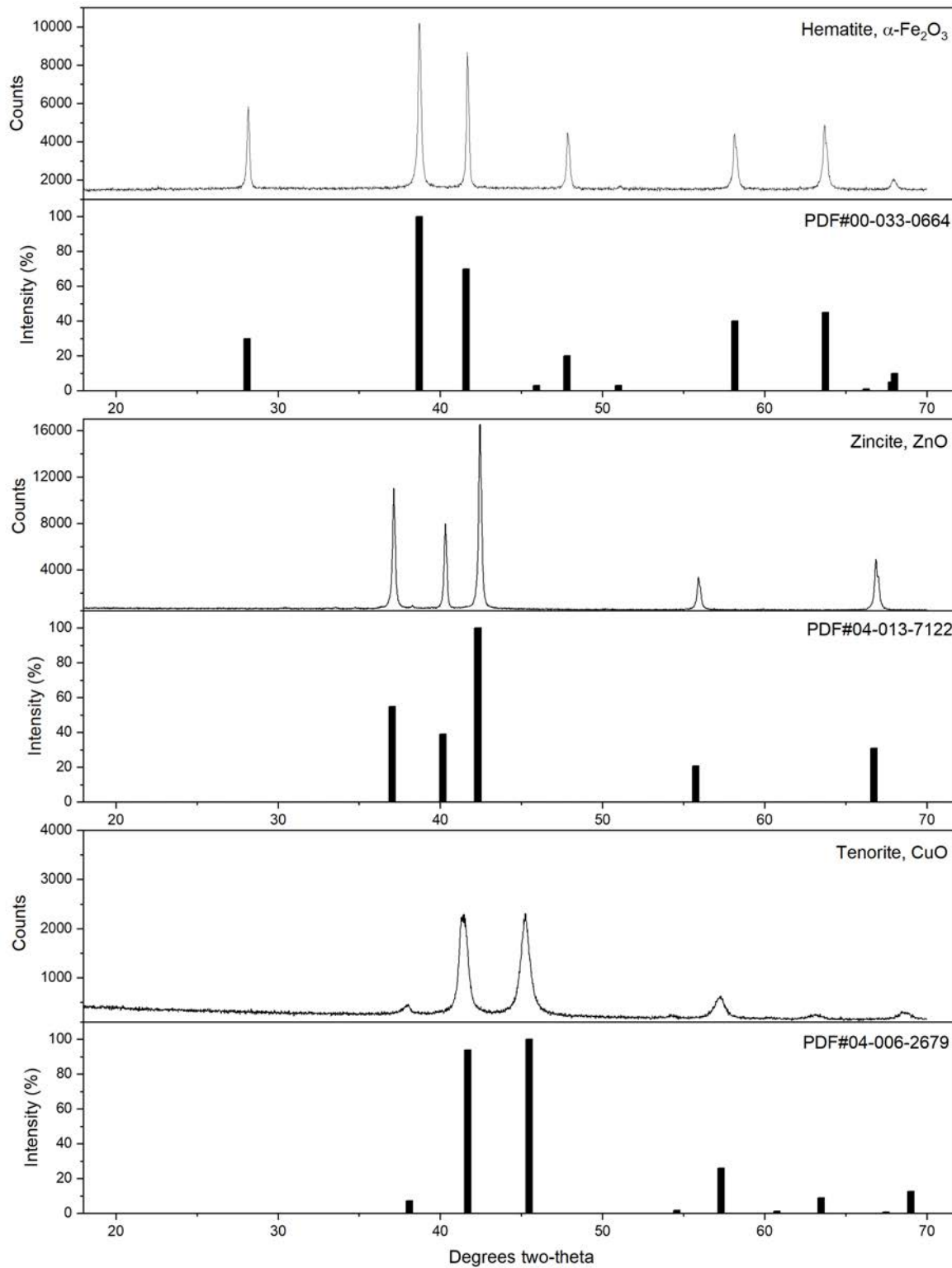
Figure S3. Phase analysis by powder X-ray diffraction on the three photo-active transition metal oxides studied in this work.

BANDGAP DETERMINATION

The reflectance (*R*) spectra was analyzed with the Kubelka-Munk function (Eq. S1) and Tauc plots to calculate the bandgap of the transition metal oxide materials. In short, the K-M function is used to make Tauc plots, which are constructed as $F(R) * E^2$ for direct and $F(R) * E^{1/2}$ for indirect energy transitions. Upon plotting these constructions versus energy, the bandgap is found from the energy intercept from extrapolation of the linear region of the plot (Fig. S4).

$$F(R) = \frac{1-R^2}{2R}$$

Eq. S1
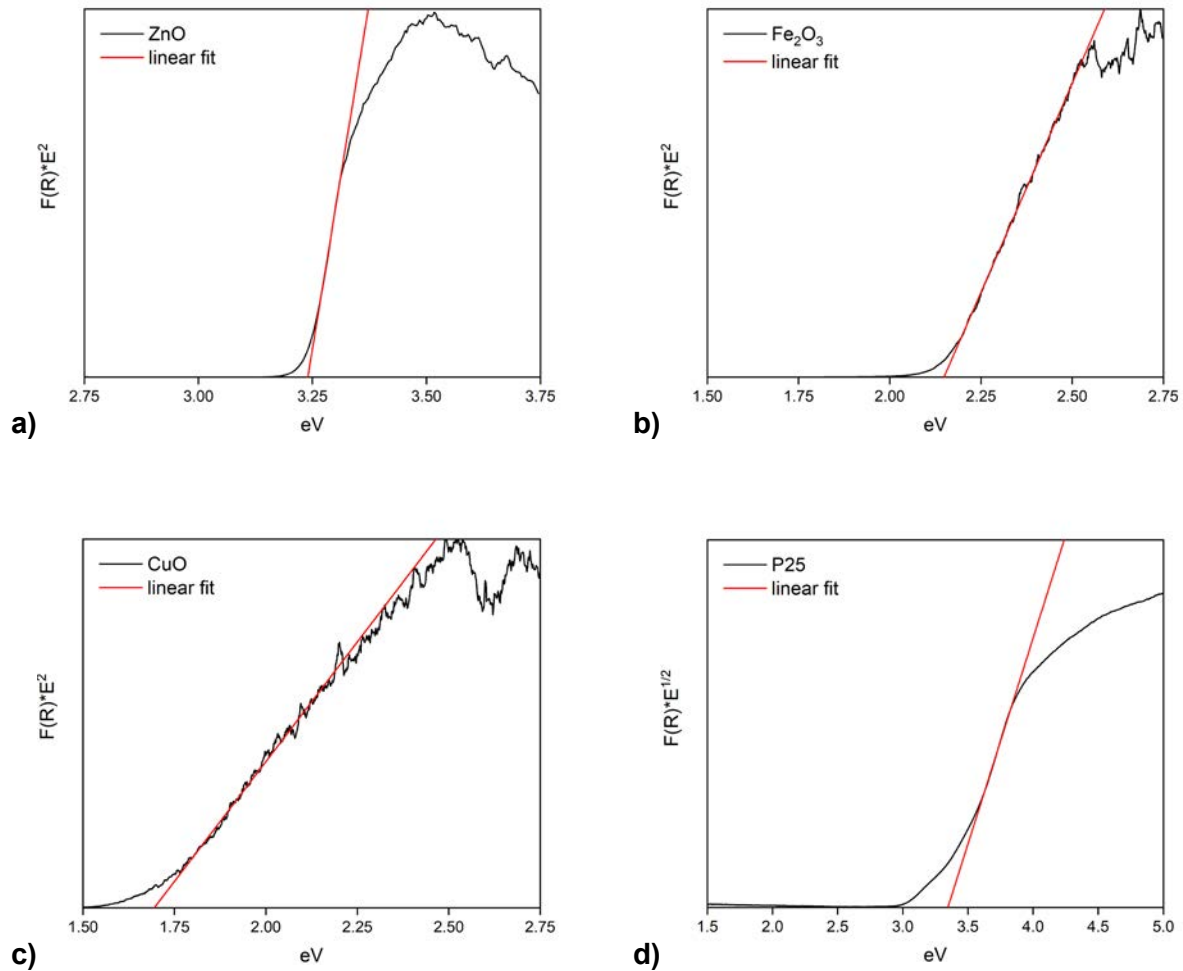
Figure S4. Tauc plots of diffuse reflectance data for the determination of band gap of the transition metal oxide materials: (*a*) ZnO, (*b*) Fe_2O_3, (*c*) CuO, and (*d*) TiO_2. Note: The P25 (TiO_2) material was treated as indirect gap due to the mixed phase (rutile, anatase) nature of this material.

PHOTOCATALYST SIZE ANALYSIS:
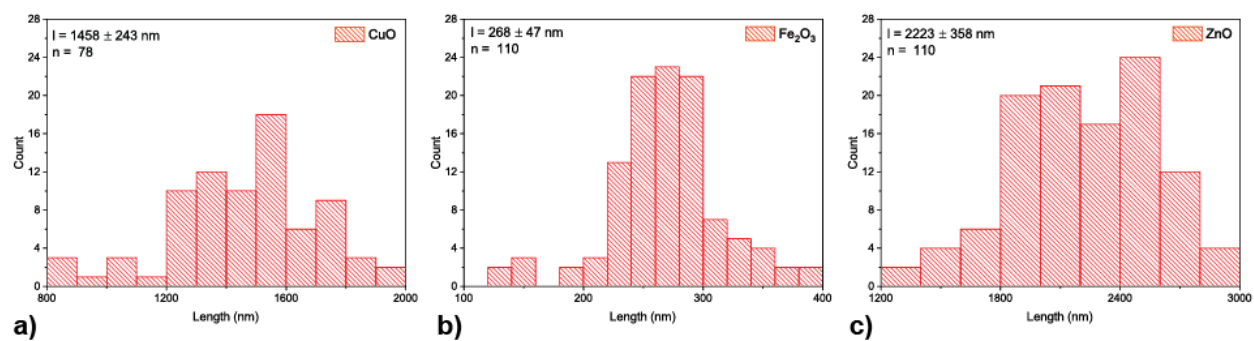
Figure S5. Particle-size distributions obtained from image analysis of SEM micrographs of each transition metal photocatalyst: (*a*) CuO, (*b*) Fe$_2$O$_3$, and (*c*) ZnO.

PHOTOCATALYTIC EXPERIMENTS:
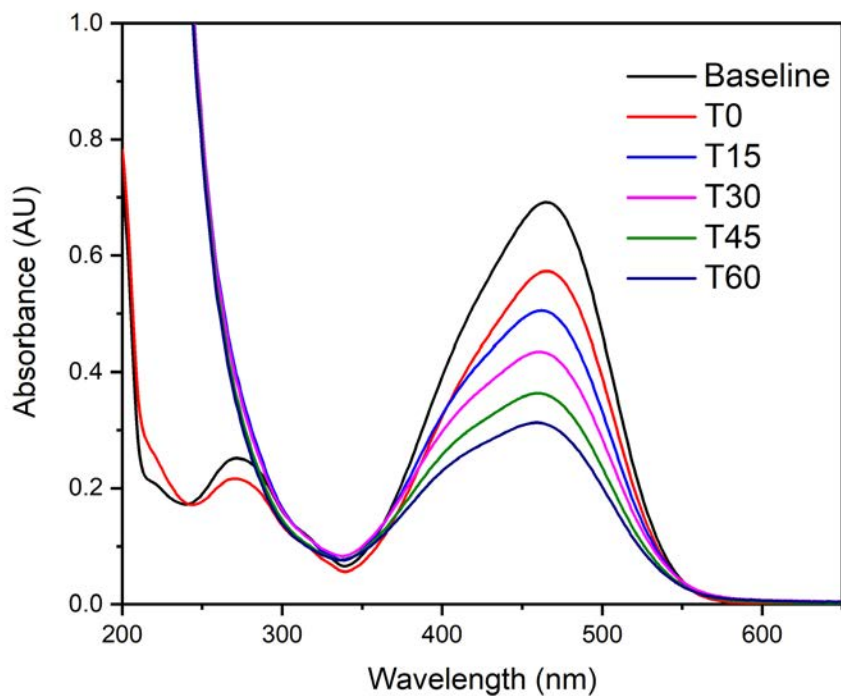
Figure S6. A representative UV-Vis Spectrum of methyl orange (MO) degradation by transition metal oxide (TMO) photocatalysts; Fe_2O_3 shown here. The initial MO concentration is 25 μM. Solution volume was 40 mL with 30 mg photocatalyst. The baseline sample represents the MO solution prior to stirring with the photocatalyst, and T0 represents the MO after 15 min stirring with photocatalyst, prior to illumination. Hydrogen peroxide (100 μL of 30%) was added immediately after the T0 sample was taken.
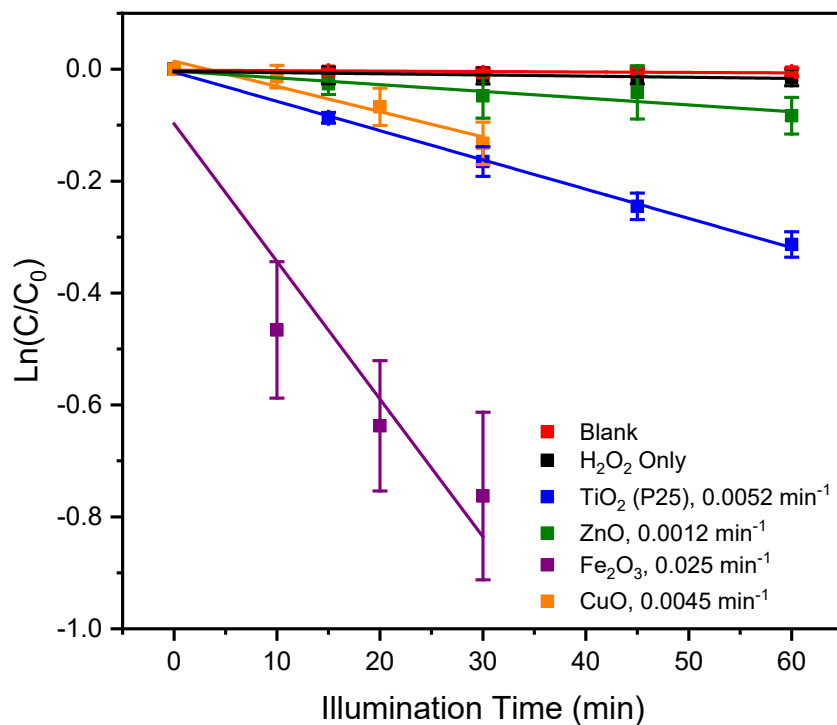
Figure S7. First-order rate-constant plots for the degradation of MO with the individual photo-active TMO materials, shown in reference to (commercial, P25) TiO_2. Slope values are equivalent to the first-order rate constants and are included in the legend. For more information, see Table 2 of the main text. Experiments designated as "Blank" were conducted with illumination only (no TMO, no hydrogen peroxide). Experiments designated as H_2O_2 were conducted with hydrogen peroxide under illumination (no TMO). All experiments were conducted with 40 mL of 25 μM MO; all experiments except TiO_2 contained 100 μL hydrogen peroxide (30%).

Table S1. Mole fraction and rate values from triaxial blend studies on photocatalyst combinations

Mole Fraction			Rate Constant (k)	
ZnO	Fe$_2$O$_3$	CuO	min^{-1}	error
0.25	0	0.75	0.0032	0.0004
0.50	0	0.50	0.0050	0.0005
0.75	0	0.25	0.0013	0.0002
0.66	0.34	0	0.0115	0.0001
0	0.14	0.86	0.019	0.001
0	0.33	0.67	0.024	0.001
0.33	0.33	0.33	0.020	0.001
0.40	0.20	0.40	0.02	0.002
0	1	0	0.025	0.006
0	0	1	0.0045	0.0008
0	0.50	0.50	0.0208	0.002
1	0	0	0.0012	0.002
0	0.80	0.20	0.041	0.003
0.20	0.80	0	0.0079	0.0003
0	0.58	0.42	0.038	0.002
0.19	0.20	0.60	0.027	0.004
0.22	0.57	0.213	0.039	0.003
0.58	0.21	0.21	0.019	0.002
0	0.72	0.28	0.045	0.005
0	0.84	0.156	0.041	0.003
0.145	0.85	0	0.0079	0.0003

Notes: All 30 mg (30.3(8)) mg, 40 mL of 25 µM methyl orange solution, 100 µL H$_2$O$_2$.

Table S2. Actual values from Fe_2O_3-CuO variable mass study

Mass Fe_2O_3 (mg)	Mass CuO (mg)	Rate Constant (k) (min^{-1})	Rate Constant Error (min^{-1})
0	15	0.0046	0.0004
10	5	0.0169	0.0005
15	7.5	0.04	0.001
20	10	0.0208	0.002
15	0	0.013	0.003
30	0	0.025	0.006
0	30	0.0045	0.0008
0	20.6	0.0051	0.0002
0	9.6	0.0036	0.0003
0	4.8	0.0033	0.0002
4.7	0	0.0058	0.0006
9.33	0	0.011	0.002
19.2	0	0.0165	0.005
15	5	0.024	0.001
15	10	0.031	0.001
15	15	0.024	0.001
27	3	0.041	0.003
7.5	22.5	0.019	0.001
22.5	7.5	0.038	0.002
20.6	20.3	0.028	0.003
0	0	0	n/a
24.7	10.1	0.033	0.001
24.6	24.7	0.031	0.002
25.4	4.97	0.045	0.005
29.5	29.4	0.033	0.003

Notes: Experiments had variable total mass TMO combinations with 40 mL of 25 µM methyl orange and 100 µL H_2O_2 (30%).
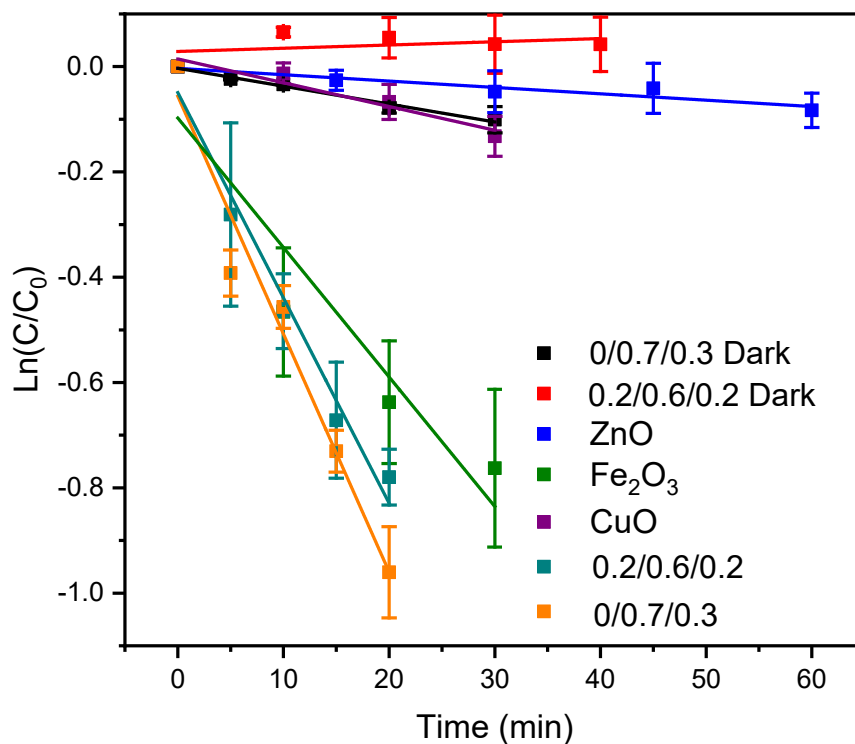
Figure S8. First-order MO degradation kinetics observed with the photocatalytic materials in combination compared against the kinetics of individual photocatalysts. Slope values are equivalent to the first-order rate constant and are compiled in the legend. For more information, see Figure S7 and Table 3 of the main text. Experiments were conducted with 40 mL of 25 μM methyl orange and 100 μL H_2O_2 (30%).

HYDROXYL RADICAL STUDIES:
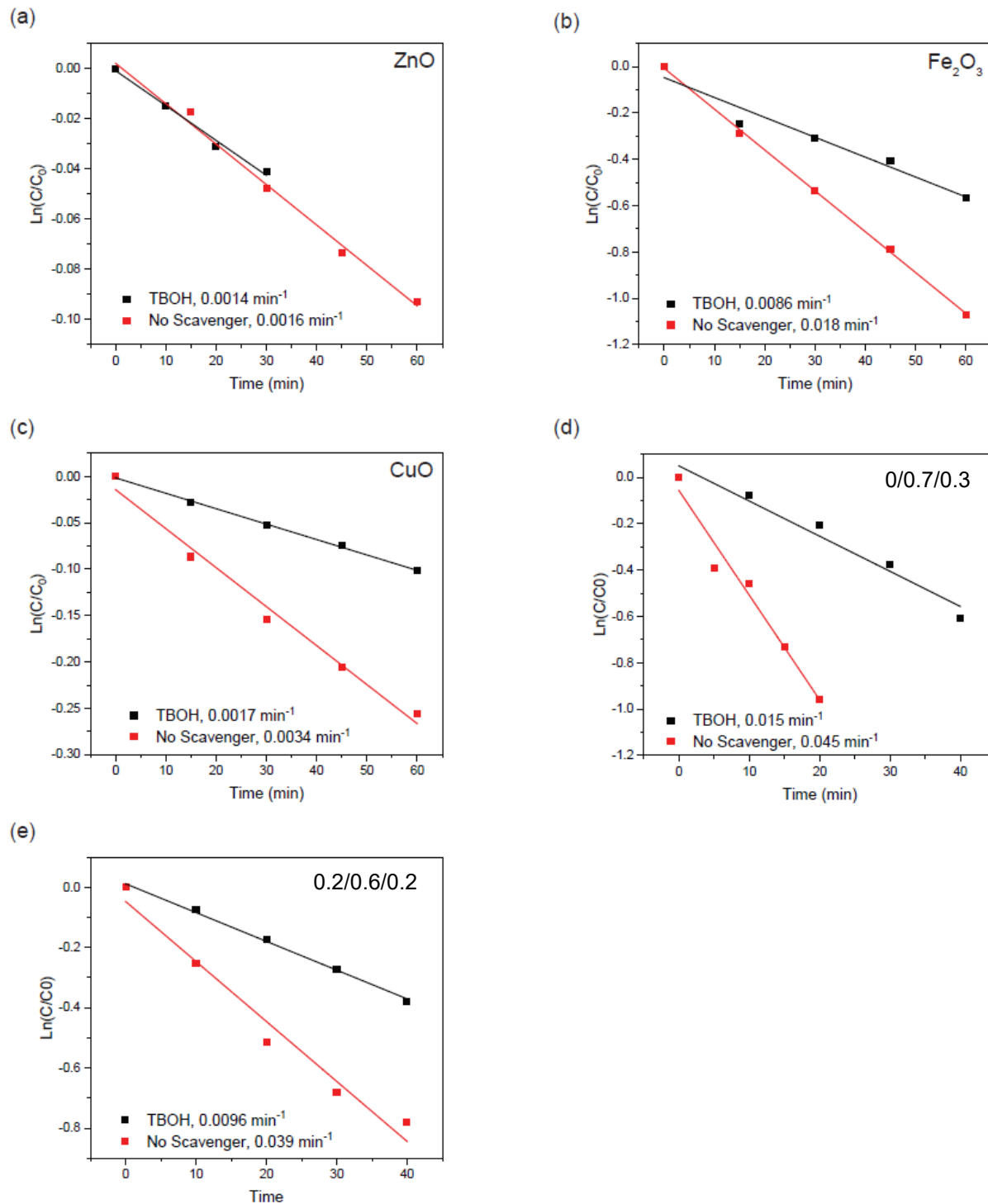
Figure S9. First-order MO degradation kinetics with individual photocatalysts and photocatalyst mixtures, with and without hydroxyl radical scavenger *tert*-butanol (TBOH). (*a*) ZnO, (*b*) Fe$_2$O$_3$, (*c*) CuO, (*d*) 7:3, and (*e*) 1:3:1.

Table S3. Rate values for scavenging experiments show in Figures 4 and S9.

Material	Rate w/out TBuOH	Rate w/TBuOH	% Reduction
ZnO	0.0016(1)	0.0014(1)	12.5
Fe_2O_3	0.018(1)	0.0086(1)	52.2
CuO	0.0034(2)	0.0017(1)	50.0
7:3	0.045(5)	0.015(4)	66.7
1:3:1	0.039(3)	0.0096(1)	75

Note: individual TMO scavenging experiments were conducted using 15 mg of each photocatalyst material.

REPORT DOCUMENTATION PAGE		*Form Approved* *OMB No. 0704-0188*

Public reporting burden for this collection of information is estimated to average 1 hour per response, including the time for reviewing instructions, searching existing data sources, gathering and maintaining the data needed, and completing and reviewing this collection of information. Send comments regarding this burden estimate or any other aspect of this collection of information, including suggestions for reducing this burden to Department of Defense, Washington Headquarters Services, Directorate for Information Operations and Reports (0704-0188), 1215 Jefferson Davis Highway, Suite 1204, Arlington, VA 22202-4302. Respondents should be aware that notwithstanding any other provision of law, no person shall be subject to any penalty for failing to comply with a collection of information if it does not display a currently valid OMB control number. **PLEASE DO NOT RETURN YOUR FORM TO THE ABOVE ADDRESS.**

1. REPORT DATE *(DD-MM-YYYY)* September 2021	2. REPORT TYPE Final	3. DATES COVERED *(From - To)*

4. TITLE AND SUBTITLE CuO Enhances the Photocatalytic Activity of Fe_2O_3 through Synergistic Reactive Oxygen Species Interactions	5a. CONTRACT NUMBER
	5b. GRANT NUMBER
	5c. PROGRAM ELEMENT NUMBER 622720048

6. AUTHOR(S) Emily Asenath-Smith, Emma K. Ambrogi, Eftihia Barnes, Jonathon A. Brame	5d. PROJECT NUMBER
	5e. TASK NUMBER
	5f. WORK UNIT NUMBER

7. PERFORMING ORGANIZATION NAME(S) AND ADDRESS(ES) U.S. Army Engineer Research and Development Center Cold Regions Research & Engineering Laboratory Geotechnical & Structures Laboratory 72 Lyme Road Environmental Laboratory Hanover, NH 03755 3909 Halls Ferry Road Vicksburg, MS 39180	8. PERFORMING ORGANIZATION REPORT NUMBER ERDC MP-21-15

9. SPONSORING / MONITORING AGENCY NAME(S) AND ADDRESS(ES) Assistant Secretary of the Army for Acquisition, Logistics and Technology Washington, DC 20314	10. SPONSOR/MONITOR'S ACRONYM(S)
	11. SPONSOR/MONITOR'S REPORT NUMBER(S)

12. DISTRIBUTION / AVAILABILITY STATEMENT

Approved for public release; distribution is unlimited.

13. SUPPLEMENTARY NOTES
This article was originally published online in the *International Journal of Colloids and Surfaces A* on 260 June 2020.
Funding was under ERDC 6.2 Advanced Low Logistics Water (ALL-H2O), Task 6: catalytic coatings, PE 622720048.

14. ABSTRACT

Iron oxide (α-Fe2O3, hematite) colloids were synthesized under hydrothermal conditions and investigated as catalysts for the photodegradation of an organic dye under broad-spectrum illumination. To enhance photocatalytic performance, Fe2O3 was combined with other transition-metal oxide (TMO) colloids (e.g., CuO and ZnO), which are sensitive to different regions of the solar spectrum (far visible and ultraviolet, respectively), using a ternary blending approach for compositional mixtures. For a variety of ZnO/Fe2O3/CuO mole ratios, the pseudo-first-order rate constant for methyl orange degradation was at least double the sum of the individual Fe2O3 and CuO rate constants, indicating there is an underlying synergy governing the photocatalysis reaction with these combinations of TMOs. A full compositional study was carried out to map the interactions between the three TMOs. Additional experiments probed the identity and role of reactive oxygen species and elucidated the mechanism by which CuO enhanced Fe2O3 photodegradation while ZnO did not. The increased photocatalytic performance of Fe2O3 in the presence of CuO was associated with hydroxyl radical ROS, consistent with heterogeneous photo-Fenton mechanisms, which are not accessible by ZnO. These results imply that low-cost photocatalytic materials can be engineered for high performance under solar illumination by selective pairing of TMOs with compatible ROS.

15. SUBJECT TERMS

Transition-metal oxide, Photocatalysis, Reactive oxygen species (ROS), Advanced oxidation processes (AOP), Colloidal, Heterogeneous photo Fenton

16. SECURITY CLASSIFICATION OF:			17. LIMITATION OF ABSTRACT	18. NUMBER OF PAGES	19a. NAME OF RESPONSIBLE PERSON
a. REPORT Unclassified	b. ABSTRACT Unclassified	c. THIS PAGE Unclassified	UU	25	19b. TELEPHONE NUMBER *(include area code)*

Standard Form 298 (Rev. 8-98)
Prescribed by ANSI Std. 239.18